Probability-based diagnostic imaging using hybrid features extracted from ultrasonic Lamb wave signals

Probability-based diagnostic imaging using hybrid features extracted from ultrasonic Lamb wave signals

Chao Zhou, Zhongqing Su and Li Cheng

Department of Mechanical Engineering, The Hong Kong Polytechnic University, Kowloon,
Hong Kong SAR

E-mail: MMLCHENG@inet.polyu.edu.hk

Abstract

The imaging technique based on guided waves has been a research focus in the field of damage
detection over the years, aimed at intuitively highlighting structural damage in two- or
three-dimensional images. The accuracy and efficiency of this technique substantially rely on
the means of defining the field values at image pixels. In this study, a novel probability-based
diagnostic imaging (PDI) approach was developed. Hybrid signal features (including temporal
information, intensity of signal energy and signal correlation) were extracted from ultrasonic
Lamb wave signals and integrated to retrofit the traditional way of defining field values. To
acquire hybrid signal features, an active sensor network in line with pulse–echo and pitch–catch
configurations was designed, supplemented with a novel concept of 'virtual sensing'. A hybrid
image fusion scheme was developed to enhance the tolerance of the approach to measurement
noise/uncertainties and erroneous perceptions from individual sensors. As applications, the
approach was employed to identify representative damage scenarios including L-shape
through-thickness crack (orientation-specific damage), polygonal damage (multi-edge damage)
and multi-damage in structural plates. Results have corroborated that the developed PDI
approach based on the use of hybrid signal features is capable of visualizing structural damage
quantitatively, regardless of damage shape and number, by highlighting its individual edges in
an easily interpretable binary image.

(Some figures may appear in colour only in the online journal)

1. Introduction

Many engineering assets including aircraft, civil infrastructure
and pressure vessels are serving in adverse working conditions,
entailing regular and timely integrity evaluation over their
lifespan. Traditional nondestructive evaluation (NDE) (e.g.
radiography, acoustic holography and infrared thermography)
requires downtime of an asset for such an inspection. In
contrast, structural health monitoring (SHM) uses permanently
installed sensors for real-time and continuous surveillance on
integrity of an asset during its normal operation. Such a
technique revamps the conventional maintenance philosophy,
therefore attracting more and more attention. Successful
implementation of SHM can increase operational efficiency,
improve reliability, reduce exorbitant maintenance costs and

extend the residual service life of ageing assets. In this aspect,
Lamb waves, the modality of guided waves in thin plate-
or shell-like structures, have been increasingly employed to
develop various SHM techniques [1–9].

As an elastic disturbance disseminated omnidirectionally
and rapidly in a medium, Lamb waves possess the capability
of interrogating local properties of the medium in a prompt
manner, outperforming local NDE techniques which are quite
labour-intensive and time-consuming due to the point-to-point
scanning fashion. Operated in an ultrasonic frequency range,
short wavelengths (of the order of a few millimetres) endow
Lamb waves to access damage of small dimensions, while
this task can hardly be satisfactorily fulfilled by other SHM
methods capitalizing on global structural features such as
eigenfrequencies or modal curvature. Therefore, Lamb-wave-

based SHM offers an outstanding compromise between local NDE and global SHM in terms of resolution, practicality and detectability.

When implementing Lamb-wave-based SHM, actuators and sensors often form a sensor network to be affixed to the structure under inspection. They work collaboratively to generate and receive ultrasonic Lamb waves, from which various signal features associated with the damage are extracted. However, in practice the signals are prone to contamination by measurement noise and uncertainties, posing difficulty in feature extraction. Moreover, Lamb waves are inherently of a dispersive and multimodal nature. All of these make interpretation of captured Lamb wave signals and feature extraction a highly challenging task, and sometimes this task can be a very subjective manner depending on individual operators.

To tackle these deficiencies, there has been increasing interest in introducing imaging techniques to Lamb-wave-based SHM. The ultimate output of an imaging technique is an easily interpretable and intuitive image reflecting the overall 'health' status of the inspected structure. Often operated in an automatic manner, this technique can efficiently minimize the dependence on subjective interpretation of signals by individual operators. Nevertheless, traditional imaging approaches, typified by Lamb wave tomography [10–12], often require dense wave paths for image reconstruction. This results in either rotation of the inspected object by very tiny increments or use of a large number of deliberately allocated transducers, fairly narrowing the application domain of imaging techniques for SHM.

To enhance the practicality of Lamb-wave-based SHM in conjunction with the use of imaging techniques, alternative methods have been explored, exemplified by a recent breakthrough: probability-based diagnostic imaging (PDI). A PDI method attempts to describe a damage event using a binary greyscale image. The field value at each image pixel is linked with the probability of damage presence at the spatial point of the inspected structure that exclusively corresponds to this pixel [13]. Most prevailing damage detection and SHM techniques define identified damage using deterministic parameters (e.g. coordinates of damage location and size of damage). Rather than using deterministic parameters, PDI presents damage in terms of its presence probability. This is deemed as an improvement over the traditional way to represent results because damage detection is actually a procedure of 'predicting' something unknown. Thus identification results should ideally be delivered using 'probability' associated with damage presence, because the underlying significance of 'probability' is more consistent with the manner of 'predicting'. Representatively, temporal-information-based PDI [14–20] converts the arrival time of damage-scattered wavepackets to spatial loci reflecting the possibility of damage occurrence, and subsequently applies geometric triangulation to locate the damage. Signal-correlation-based PDI [21–23] hypothesizes that a low correlation between two signals captured from a damaged structure and from its intact counterpart implies a high probability of damage presence along the signal acquisition

path and vice versa. Based on this, the damage can be located by seeking intersections of several paths along which the captured signals exhibit low correlation. Phased-array-based PDI [22, 24] uses the superposition of wavefronts generated by a series of arrayed sensors, sequentially activated with time delays, to scan the entire inspection area and locate damage if additional signal scattering is captured.

In spite of the fact that most approaches in this field have the capacity of locating damage, quantitative depiction of damage including its shape and size is still among those highly challenging tasks. This difficulty is particularly accentuated for orientation-specific damage of sizeable length in a particular dimension (e.g. a crack or a notch) because such sort of damage exerts strong directivity to wave propagation and, as a consequence, the damage-scattered waves may not be captured efficiently at certain sensing locations in the absence of prior knowledge on damage orientation.

A novel PDI approach in conjunction with the use of hybrid signal features was developed, based on relationships between (i) temporal information and damage location, (ii) intensity of signal energy and damage orientation/shape and (iii) signal correlation and damage location/severity. An active sensor network in conformity to pulse–echo and pitch–catch configurations was designed, supplemented with a novel concept—'virtual sensing', to capture hybrid signal features. The approach was validated by predicting representative damage scenarios including L-shape through-thickness crack (orientation-specific damage), polygonal damage (multi-edge damage) and multi-damage in aluminum plates.

2. Probability-based diagnostic imaging (PDI) using hybrid signal features

In most PDI approaches, the planar area of an inspected structure is first meshed and projected to an image, each image pixel corresponding exclusively to a spatial point of the structure. The value of an image pixel is termed field value in what follows, which can be linked to the probability of damage presence at the spatial point of the structure corresponding to that pixel, using appropriately extracted signal features.

In this study, various signal features were extracted from captured Lamb wave signals for establishing different genres of field value using different mechanisms, which were then fused using a hybrid fusion scheme. The basic philosophy of this proposed PDI technique is illustrated in figure 1. In particular it is noteworthy that the hybrid fusion of various genres of field value as indicated in the figure was developed based on thorough consideration of the mathematical properties of individual fusion schemes, rather than simply stacking all available information together. Therefore this hybrid fusion exercise has solid and explicit justification for each step (to be addressed in section 3).

To acquire various signal features associated with damage, an active sensor network in conformity to the pulse–echo and pitch–catch configurations was designed. Pulse–echo and pitch–catch are two configurations for allocating the sensor and actuator in a sensing path. In the former, a sensor collocated with the actuator is used to 'listen to' the wave
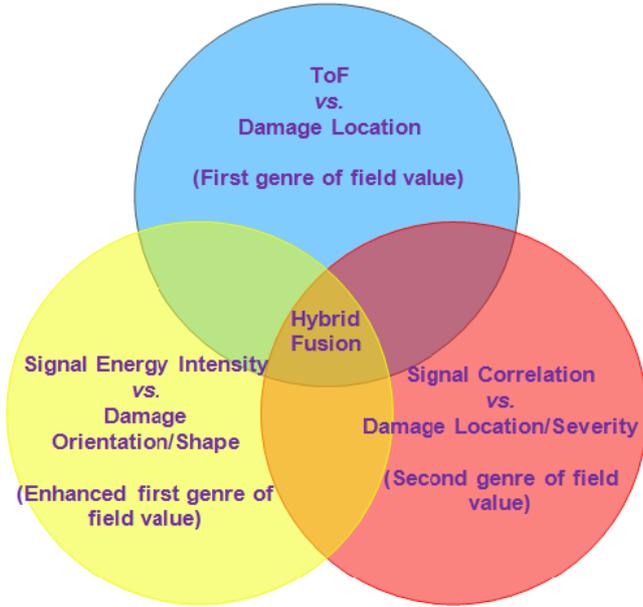
Figure 1. Basic philosophy of the proposed PDI approach using hybrid signal features and a hybrid fusion scheme.

Figure 2. Relative positions among actuator A_i, sensor S_i and damage in the local coordinate system for sensing path $A_i - S_i$.

echoed back from the damage upon interaction between the incident wave and the damage; while in the latter, an incident signal is activated by the actuator to propagate across the object under inspection and a sensor at the far-field of the object receives the damage-scattered waves. In this study, both configurations were used to generate different genres of field values, respectively.

2.1. Time-of-flight (ToF)-based field value (first genre of field value)

ToF, defined as the time consumed for a wavepacket to travel a certain distance, is one of the most straightforward features of a wave signal. Consider a sensor network consisting of N pulse–echo pairs. For a given pulse–echo pair, $A_i - S_i$ ($i = 1, 2, \ldots, N$, A_i serves as the actuator and S_i the sensor), a local coordinate system can be established in which the origin is between A_i and S_i, and the damage centre is presumed to be at (x_D, y_D), as sketched in figure 2. Provided the propagation velocity V of the selected wave mode is constant before and after interaction with the damage, there exists a set of nonlinear equations for the entire sensor network:

$$\frac{L_{A_i-D} + L_{D-S_i}}{V} = \Delta t_i \qquad (i = 1, 2, \ldots, N), \quad (1)$$

where Δt_i is the sum of (i) the ToF for the incident wave to propagate from A_i to the damage and (ii) the ToF for the damage-reflected wave to propagate from damage to S_i. L_{A_i-D} and L_{D-S_i} represent the distances between A_i and the damage, and the damage and S_i, respectively. Because the distance between A_i and S_i is much smaller than L_{A_i-D} and L_{D-S_i}, it can be hypothesized that $L_{A_i-D} = L_{D-S_i} = \sqrt{x_D^2 + y_D^2}$. Mathematically, equation (1) depicts a series of circle-like loci, indicating possible damage locations. Each locus is namely the
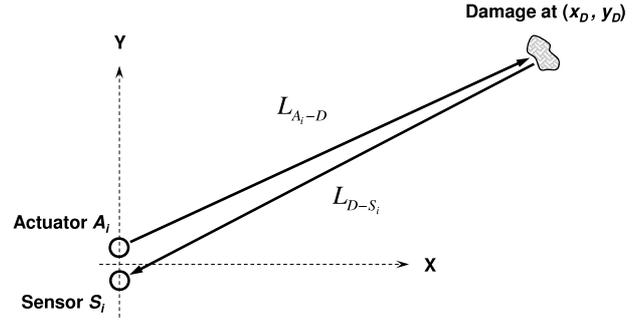
prior perceptions regarding the presence of damage from the perspective of the pulse–echo pair which creates such a locus.

Further, we mesh the inspected planar area using $K \times L$ nodes virtually. It is understandable that the mesh nodes right-located on an above-established locus have the highest degree of probability of damage presence; for the others, the greater the distance to the locus the lower the probability damage exists there. To quantify the probabilities at all nodes with regard to all loci, a cumulative distribution function, $F(z_i)$, is introduced, defined by [13]

$$F(z_i) = \int_{-\infty}^{z_i} f(z) \cdot dz, \quad (2)$$

where $f(z) = \frac{1}{\sigma_i \sqrt{2\pi}} \exp[-\frac{z^2}{2\sigma_i^2}]$ is the Gaussian distribution function, representing the probability density of damage presence at mesh node (x_m, y_n) ($m = 1, 2, \ldots, K; n = 1, 2, \ldots, L$), established by sensing pair $A_i - S_i$. $z_i = \|\chi_i - \mu_i\|$, where χ_i is the location vector of node (x_m, y_n) and μ_i is the location vector of the point on the locus created by $A_i - S_i$ that has the shortest distance to (x_m, y_n). σ_i is the standard variance and is selected based on a series of trials. Given a distance, z_i, the probability of damage presence at (x_m, y_n), $I(x_m, y_n)$, established by sensing path $A_i - S_i$, becomes

$$I(x_m, y_n)|_{\mathrm{I}} = 1 - [F(z_i) - F(-z_i)]. \quad (3)$$

The probability of damage presence at node (x_m, y_n), defined by equation (3), can be illustrated in figure 3. In the figure, the x axis refers to the distance between a spatial node and a root locus, while the y axis refers to the probability density. The dark region represents the probability density of the structure being completely healthy at the discussed spatial node, whereas two white regions represent the probability density of the structure being in possession of damage at the discussed node. When z_i reaches zero (the discussed node is right located on the established root locus), the dark region retreats to zero. In equation (3), subscript I stands for the first genre of field value in the approach that is based on sole ToF-related signal features. Figure 4 exemplarily displays a probability image obtained using equation (3), where the lighter the greyscale, the greater the possibility of damage existing at that pixel (each pixel exclusively corresponds to a spatial point of the structure under inspection).
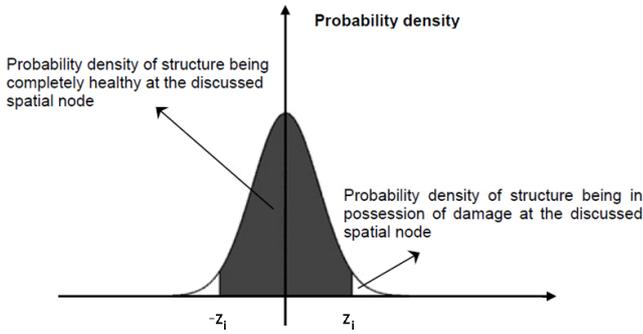
Figure 3. Normal distribution of the probability density with regard to the presence of damage at a specific spatial node of the structure under inspection.
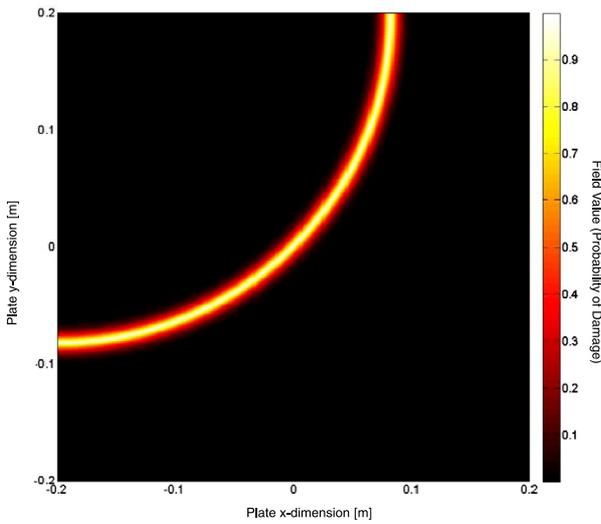

Figure 4. A typical probability image established by a sensing path using the first genre of field value (diagram showing inspection area only covered by the sensor network).

Figure 5. Intensity of signal energy (A_0 mode) reflected by a crack *vs.* angle of wave incidence (dotted line: FE simulation results, solid line: experimental results; normalized by the magnitude of damage-reflected wave at a normal incidence $\theta = 0°$).

where $I(x_m, y_n)'|_I$ is the enhanced first genre of field value at pixel (x_m, y_n). Ξ is the intensity of damage-reflected wave energy which has already been compensated for wave attenuation as propagation distance using $f'(t) = f(t) \cdot \frac{\sqrt{d}}{\sqrt{d_0}}$ ($f'(t)$ and $f(t)$ are the compensated and original wave signals, respectively; d and d_0 are the propagation distances at which the wave signal is captured and a reference distance [25]). Ξ_{max} is the extremum of Ξ obtained via all available actuator–sensor pairs in the sensor network. Integrating (i) intensity of damage-reflected wave energy, which is susceptible to damage orientation, with (ii) ToF-related information, which is sensitive to damage location, the enhanced first genre of field value is able to highlight the orientation of damage, in addition to its location.

2.2. Enhanced first genre of field value

A ToF-based field value defined by equation (3) can facilitate a procedure of locating damage, but its effectiveness in depicting damage shape, size and severity is debatable. That is because different locations of damage can lead to a significant difference in ToF of damage-scattered waves; but discrepancies in damage shape, size or severity often cause changes in temporal information at an unperceivable level only.

As concluded in the authors' previous work [25], the intensity of damage-reflected wave energy can be a sensitive indicator for damage orientation, as correlated in figure 5 in which the strongest reflection is captured with normal incidence, and with the increase of angle of wave incidence, the intensity of crack-reflected signal energy quickly decreases. Based on this, the first genre of field value was re-defined by integrating extracted signal features associated with the intensity of signal energy as

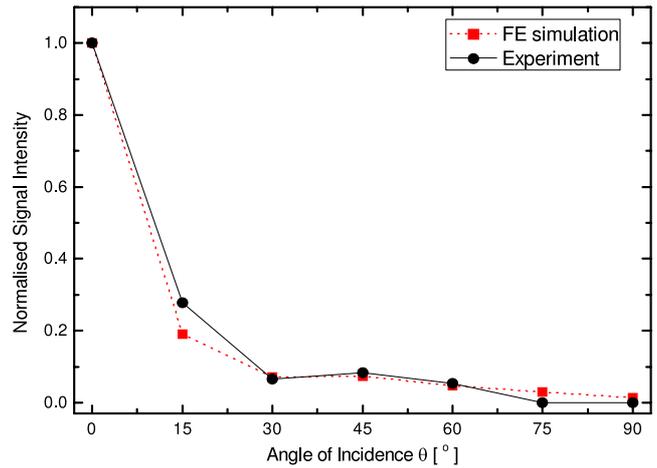$$I(x_m, y_n)'|_I = \frac{I(x_m, y_n)|_I \times \Xi}{\Xi_{max}}, \qquad (4)$$

2.3. Signal-correlation-based field value (second genre of field value)

It is appreciated that the correlation coefficient between two signals captured from the inspected structure (current signal) and from its 'healthy' counterpart (baseline signal) can quantitatively indicate changes in the structure along or near the sensing paths via which these signals are acquired. The physical intuition behind this is that a captured wave signal would change drastically if a defect right locates on or very close to its sensing path, presenting a relatively small correlation coefficient between two signals. In contrast, the signal deviation would be trivial if the defect is away from the sensing path, leading to high similarity between two signals (i.e. a great correlation coefficient). The correlation coefficient has, in particular, proven susceptibility to changes in signal phase (leading to different ToFs) as well as changes in local signal amplitude (leading to different intensities of signal energy) [26], therefore advantageous over other signal features in terms of the sensitivity to phase delay and reduction in signal amplitude. Signal features associated with signal correlation were therefore extracted in this approach to develop the second
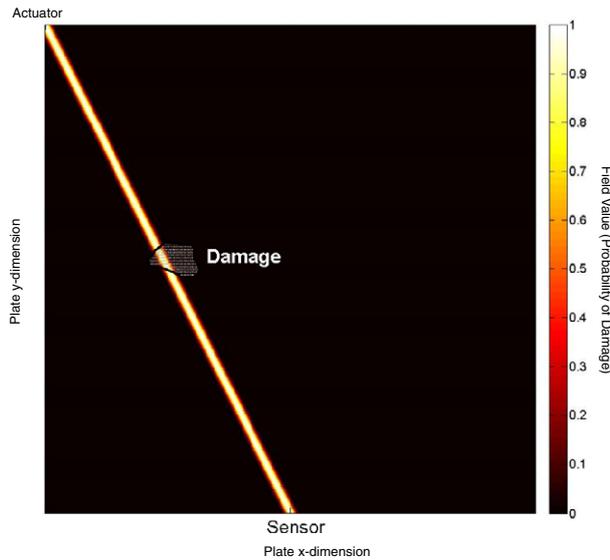
4

Figure 6. A typical probability image established by a sensing path using the second genre of field value (diagram showing inspection area only covered by the sensor network).

Figure 7. Schematic of a sensor network consisting of five physical sensing paths and a virtual sensing path.

genre of field value, in accordance with a pitch–catch sensor network configuration.

Considering two wave signals of the same length $X = \{x_1, x_2, \ldots, x_n\}$ (current signal) and $Y = \{y_1, y_2, \ldots, y_n\}$ (baseline signal) (both having n sampling points) captured via a sensing path having an angle of α relative to a pre-selected benchmark direction, the second genre of field value is defined as

$$I(\alpha)|_{\mathrm{II}} = 1 - \rho, \qquad (5)$$

where ρ is the correlation coefficient between signals X and Y, defined as

$$\rho = \frac{C_{XY}}{\tau_X \cdot \tau_Y} = \frac{\sum_{i=1}^n (x_i - \mu_X)(y_i - \mu_Y)}{\sqrt{\sum_{i=1}^n (x_i - \mu_X)^2} \cdot \sqrt{\sum_{i=1}^n (y_i - \mu_Y)^2}}. \qquad (6)$$

In the above, C_{XY} is the covariance of X and Y; τ and μ are the standard deviation and mean of the signal, respectively, distinguished by different subscripts for the two signals. Subscript II stands for the second genre of field value in the approach that is based on sole correlation-related signal features. In terms of equation (5), all the pixels along a sensing path hold the same field value. Because X and Y are two signals captured via the same sensing path in the same structure, the greater the similarity between them, the closer to unity is the coefficient, leading to low field values at pixels along this sensing path and indicating low probability of damage existence near this sensing path; in contrast, in the case damage occurs in or close to a particular sensing path, the correlation coefficient between two signals becomes low, resulting in high field values at pixels along this sensing path.

2.4. Enhanced second genre of field value

The mathematical nature of equation (6) makes a small discrepancy between two signals become magnified considerably in the correlation coefficient, and as a result the image established
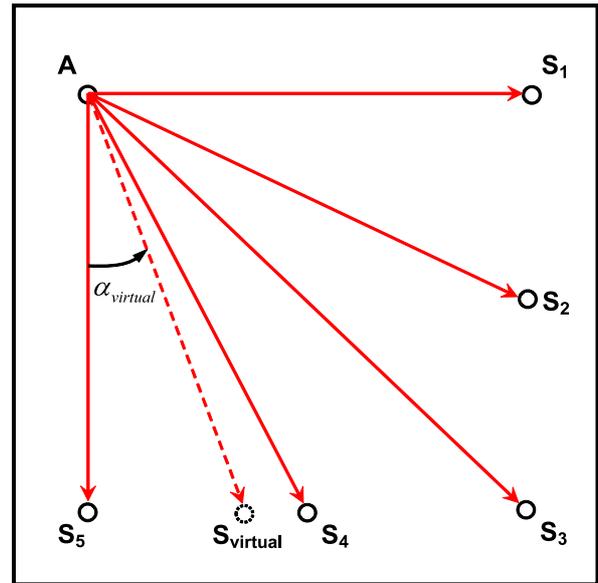
in terms of the second genre of field value often shows a very narrow band of highlight along the sensing path, if part of the damage is in the path or very close to it, while pixels at other regions of the image hold very low field values. In other words, a particular sensing path can only sense damage near it, making the field value defined by equation (5) highly inert to distant damage. By way of illustration, figure 6 presents a probability image using the second genre of field value established by a sensing path passing through damage, to observe that only those pixels along this sensing path have very high field values.

Such a trait of the second genre of field value can be beneficial to detection of multi-damage, but it poses demanding requirements on the density of sensing paths to cover the inspection area. Although introducing more sensing paths certainly helps achieve a denser coverage and enhance the ability to detect damage at more random locations, merits of the developed PDI approach over traditional tomography relying on a large number of actuator–sensor pairs are impaired fairly. To overcome this deficiency, an interpolation method based on a novel concept, 'virtual sensing', was developed, aimed at virtually generating more sensing paths but not at the expense of introducing more physical sensors. To understand, consider a sensor network comprised of an actuator, A, and five sensors, S_1, S_2, S_3, S_4 and S_5, forming five sensing paths: $A-S_1$, $A-S_2$, $A-S_3$, $A-S_4$ and $A-S_5$, shown schematically in figure 7. Knowing that the angle of each sensing path with regard to a benchmark direction (e.g. $A - S_5$) is α_1, α_2, α_3, α_4 and α_5 ($\alpha_5 = 0°$ for the current selection of benchmark directions), respectively, the second genre of field values at pixels along these five sensing paths can be calculated in terms of equation (5), leading to $I(\alpha_1)|_{\mathrm{II}}$, $I(\alpha_2)|_{\mathrm{II}}$, $I(\alpha_3)|_{\mathrm{II}}$, $I(\alpha_4)|_{\mathrm{II}}$ and $I(\alpha_5)|_{\mathrm{II}}$, respectively. Apart from those sensing paths configured by the physically existing actuator (A) and sensors (S_1, S_2, S_3, S_4 and S_5), virtual sensing paths connecting A and an imaginary sensor (S_{virtual}) located at any position of interest within the inspection area can also be formed virtually.

For the exemplificative case in figure 7, the second genre of field values at all pixels along a virtual sensing path, $A - S_{\text{virtual}}$ (with an angle of α_{virtual} relative to the benchmark direction), can be obtained using the field values of two physical sensing paths which are clockwise and anticlockwise closest to $A - S_{\text{virtual}}$, by linearly scaling their respective field values and angles, as

$$I(\alpha_{\text{virtual}})|_{\text{II}} = I(\alpha_k)|_{\text{II}} + (\alpha_{\text{virtual}} - \alpha_k)\frac{I(\alpha_{k+1})|_{\text{II}} - I(\alpha_k)|_{\text{II}}}{\alpha_{k+1} - \alpha_k}$$

$$(\alpha_{k+1} < \alpha < \alpha_k), \quad (k = 1, 2, 3, 4). \tag{7}$$

$I(\alpha_{\text{virtual}})|_{\text{II}}$ is the second genre of field value for this virtual sensing path. The same as a physical sensing path, all pixels along a virtual sensing path hold the same second genre of field value. By virtue of the concept of 'virtual sensing', the second genre of field value at all pixels across the entire inspection region, even for those areas in which there is no any physical sensing path passing through, can be determined by changing α_{virtual} by a tiny increment (1° in this study). The concept of 'virtual sensing' virtually and significantly expands the sensor network coverage without the need of more sensors.

3. Imaging fusion scheme

In terms of equations (4), (5) and (7), various signal features extracted from captured wave signals were used to develop different genres of field value. The probability image established by a sensing path, whichever genre is used, is defined as the source image hereinafter. A source image is the prior perceptions regarding damage from the viewpoint of the sensing path that creates this image. In practice, a source image contains not only information associated with damage but unwanted features such as ambient noise and measurement uncertainties, multiple wave modes and reflections from structural boundaries. These unwanted signal features possibly dim damage-associated features and weaken perceptions from individual source images. To circumvent this, image fusion was introduced in the approach. The ultimate deliverable of the fusion was a resulting image. During fusion, a pixel was considered at a time (other pixels were not considered) and the field value at this pixel in the resulting image was calculated by appropriately amalgamating corresponding field values at this pixel in individual source images.

Considering a sensor network consisting of N pairs of actuators and sensors ((A_i, S_i), $i = 1, 2, \ldots, N$) as shown in figure 8, two types of sensing configurations are available: pulse–echo ($A_i - S_i$ ($i = 1, 2, \ldots, N$)) and pitch–catch ($A_i - S_j$, ($i, j = 1, 2, \ldots, N$, but $i \neq j$)), respectively. Upon extraction of signal features (ToF, intensity of signal energy and correlation coefficients),

(i) for every single pulse–echo path, the first genre of field value (ToF-based with integrated intensity of signal energy) is calculated using equation (4). Each sensing path thus creates a source image and the one established by the ith pulse–echo path is denoted by $I'_i|_{\text{I}}$;

(ii) for every actuator A_i, the second genre of field value (correlation coefficient-based) is first calculated using equation (5), in which physically existing paths $A_i - S_j$
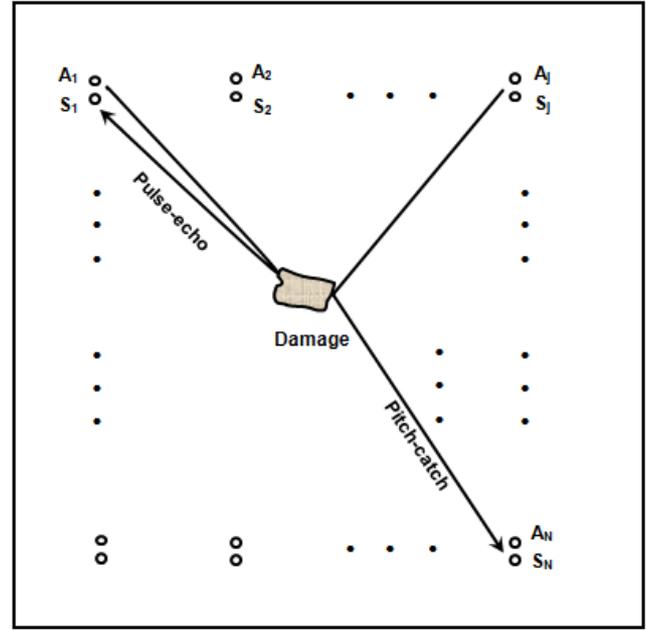

Figure 8. An active sensor network consisting of N pairs of actuator and sensor.

($j = 1, 2, \ldots, N$, but $j \neq i$) contribute $N - 1$ probability images. Subsequently, with the concept of 'virtual sensing', a series of virtual sensing paths connecting A_i with imaginary sensors at different locations are virtually formed by changing α_{virtual} with an increment of 1°. Thus, each virtual path renders a probability image as well, in accordance with the principle described by equation (7). All these probability images, from $N - 1$ physical paths and all virtual paths, are aggregated, to create a source image for the current actuator (A_i), denoted by $I_i|_{\text{II}}$.

To summarize the above, each actuator (N in total) offers a source image via pulse–echo configuration and another source image via pitch–catch configuration. Then, a hybrid fusion scheme was developed to fuse all available source images in the sensor network, as

$$P_{\text{hybrid}} = \frac{1}{N} \sum_{i=1}^{N} (I'_i|_{\text{I}} \cap I_i|_{\text{II}}), \tag{8}$$

as a flowcharted in figure 9, where P_{hybrid} is the field value in the ultimate resulting image.

The incentive to develop such a hybrid fusion scheme is twofold:

(i) an arithmetic fusion ('Σ' in equation (8)) equally takes into account all prior perceptions from source images and well-decentralizes individual contributions. Although the arithmetic fusion guarantees a full inclusion of prior perceptions from all source images, information in all source images including ambient noise and measurement uncertainty is also engaged, which might 'pessimistically exaggerate' the possibility of damage presence, leading to false alarm (pseudo damage); and
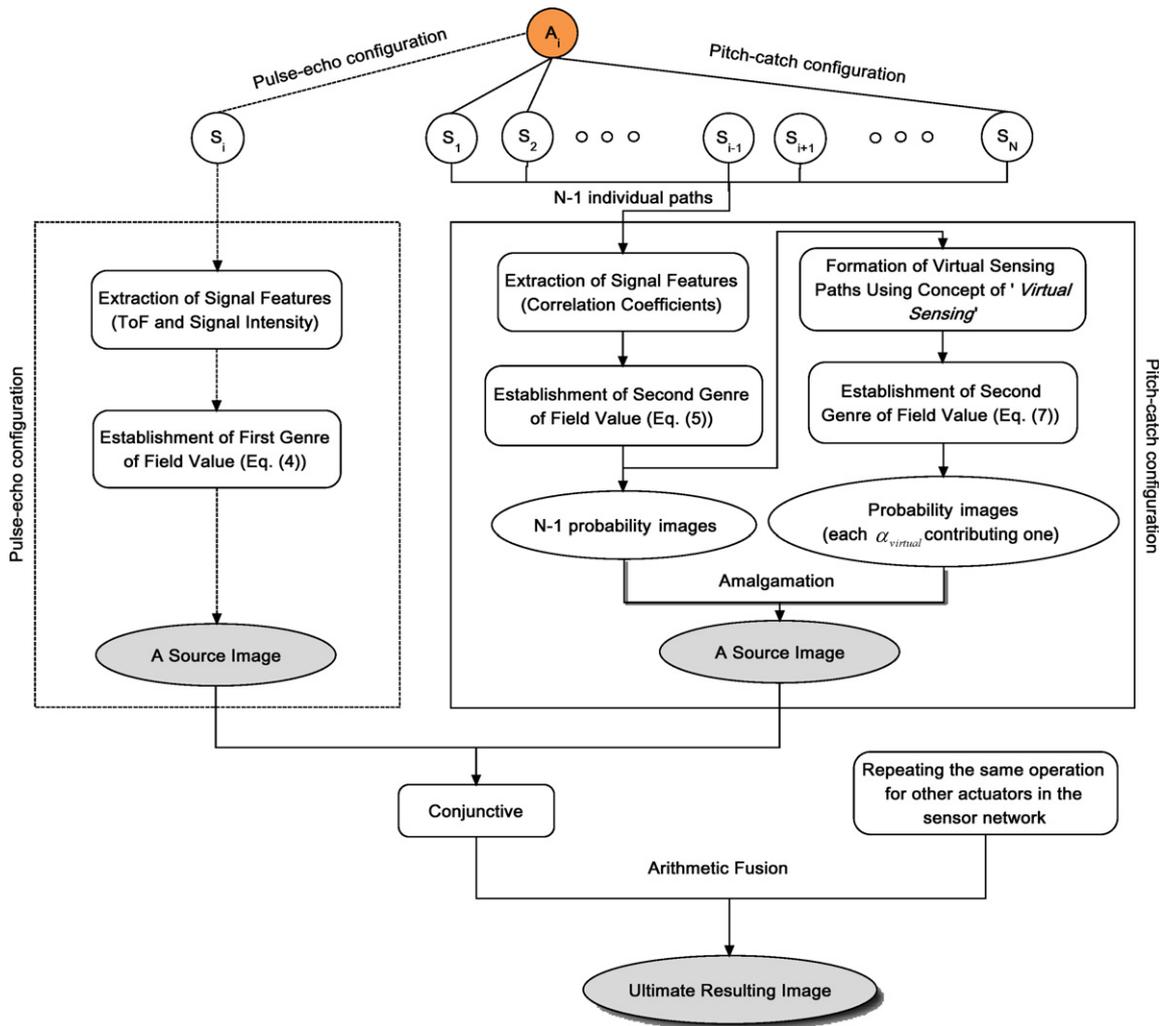
6

Figure 9. Flowchart of the proposed hybrid fusion scheme.

(ii) a conjunctive fusion ('∩' in equation (8)) multiplicatively processes source images, and a low field value at a pixel in any source image can lead to significantly low likelihood of damage presence at that pixel in the ultimate resulting image.

Through the hybrid fusion, damage-related information (commonality in individual source images) stood out and noise (random information in individual source images) is filtered.

4. Applications to structural damage identification

The developed PDI approach, active sensor network and hybrid fusion scheme were employed to identify various types of structural damage, including L-shape through-thickness crack (strong orientation-specific damage), polygonal damage (multi-edge damage) and multi-damage in aluminum plates.

4.1. L-shape crack (strong orientation-specific damage)

An aluminum plate (600 mm × 600 mm × 1.5 mm) was fixed along its four edges on a testing table, and an L-shape crack comprised of two through-thickness edges (edges I and II, each being 25 mm long and 1.5 mm wide) was introduced into the plate using a fine blade, as seen in figure 10. Sixteen circular piezoelectric lead zirconate titanate (PZT) wafers (nominal diameter: 5 mm, thickness: 0.5 mm each) were surface-mounted on the plate to form an active sensor network. Such a sensor network provided eight pulse–echo sensing paths, $A_i - S_i$ ($i = 1, 2, \ldots, 8$) and $7 \times 8 = 56$ pitch–catch sensing paths, $A_i - S_j$ ($i, j = 1, 2, \ldots, 8, i \neq j$). The diagnostic signal (Hanning-window-modulated five-cycle sinusoid tone bursts at a central frequency of 450 kHz) was generated in MATLAB® and downloaded to an arbitrary waveform generation unit (Agilent® E1441 on a VXI platform), in which D/A conversion was performed. The analogue signal was amplified to 60 V_{p-p} using a linear amplifier (PiezoSys® EPA-104) to drive each PZT actuator in turn. Wave signals were captured using an oscilloscope (HP™-54810A) at a sampling rate of 25 MHz. Shielded wires and standard BNC connectors were used to minimize measurement noise. All captured signals were normalized with regard to the magnitudes of their respective incident waves for eliminating differences in soldering and bonding for individual wafers.
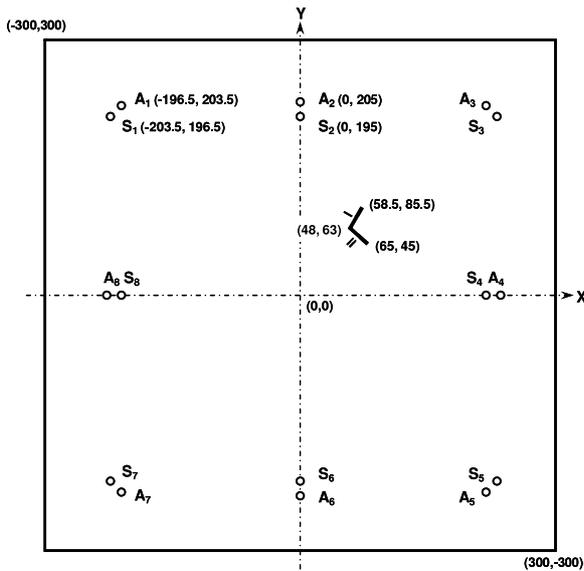
Figure 10. Specimen configuration for identifying an L-shape crack (unit: mm) (PZT wafers in the sensor network being symmetric relative to *x* and *y* axes).

As an example of signals captured via the pulse–echo configuration, figure 11(a) exemplarily displays the current and corresponding baseline signals sensed by $A_3 - S_3$. In order to obtain the first genre of field value, two signals were applied with Hilbert transform (HT) [27], in figure 11(b), whose difference is shown in figure 11(c) to strengthen an extra wavepacket scattered by the damage. In the difference signal, the damage-reflected fundamental order antisymmetric mode (A_0) can be observed explicitly (at the current selection of excitation frequency, the A_0 mode dominates, whereas the fundamental-order symmetric mode (S_0) is substantially suppressed. Accordingly, the defect-reflected S_0 mode is very weak in comparison with the defect-reflected A_0 mode, benefiting subsequent signal interpretation and feature extraction), featuring high intensity, thanks to the relatively small angle of wave incidence along $A_3 - S_3$ with regard to edge II ($\theta < 5°$). In terms of equation (4), the source image established by $A_3 - S_3$ was constructed, in figure 12. Following the same principle, each pulse–echo path in the sensor network (eight in total) respectively provided a source image.

As an example of signals captured via the pitch–catch configuration, figure 13 shows the current and corresponding baseline signals acquired by $A_2 - S_5$ to observe that magnitudes of both S_0 and A_0 modes in the current signal are much weaker than those in the baseline signal. Such a reduction in magnitude can be attributed to the fact that path $A_2 - S_5$ right-passed through a partial of the damage, and both S_0 and A_0 modes captured via this sensing path were prominently modulated by the damage. This led to a relatively small correlation coefficient ($\rho = 0.891$) between the current and baseline signals. In terms of equation (5), the second genre of field values at pixels along all physical pitch–catch paths were calculated. Further, for each actuator, the field values along all virtual sensing paths radiated from this actuator were obtained by increasing α with an increment of 1°, following the mechanism of 'virtual sensing' described by equation (7).
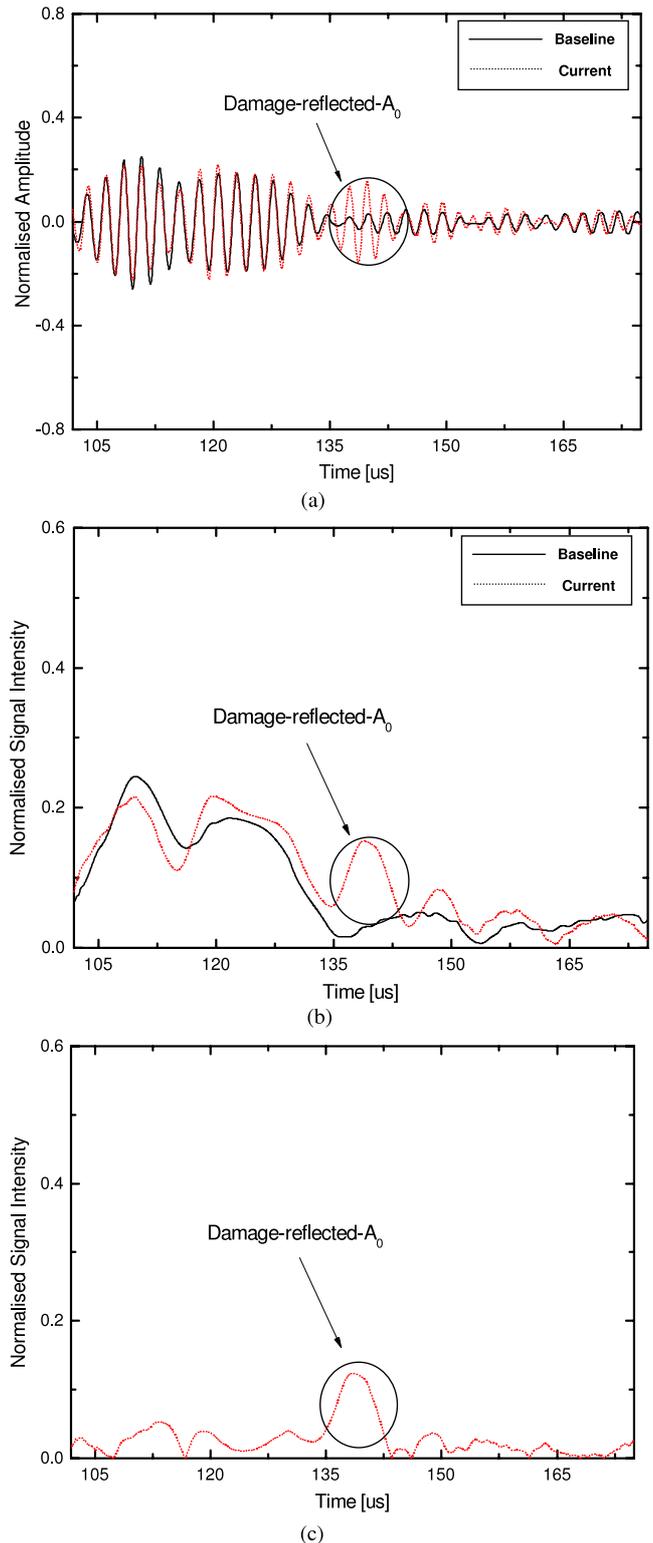

Figure 11. (a) Current and baseline signals acquired via pulse–echo sensing path $A_3 - S_3$ (normalized by the magnitude of incident waves); (b) energy distribution of signals in (a) obtained using HT and (c) difference between two signals in (b).

Every physical or virtual sensing path contributed a probability image, respectively, and all of them were aggregated for this actuator, as detailed in section 3. By way of illustration, figure 14 exhibits the probability image when A_2 served as
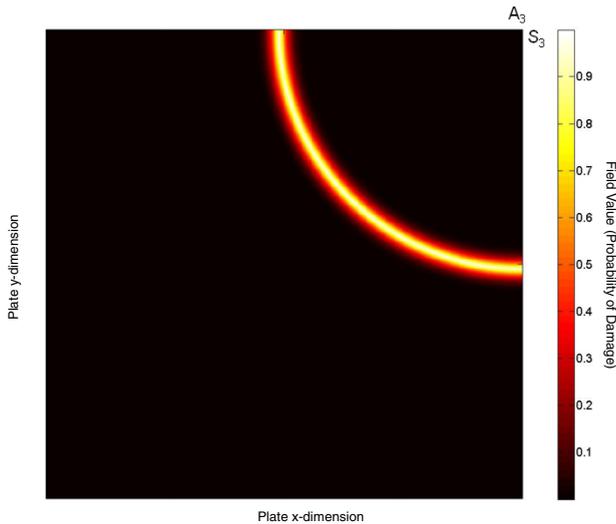
Figure 12. Source image established by $A_3 - S_3$ (diagram showing inspection area only covered by the sensor network).
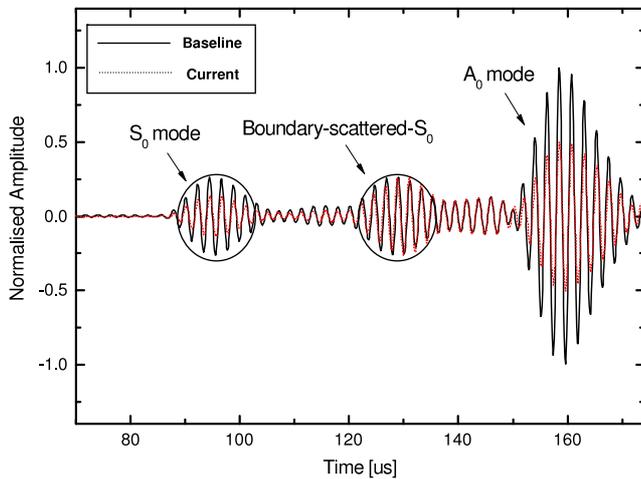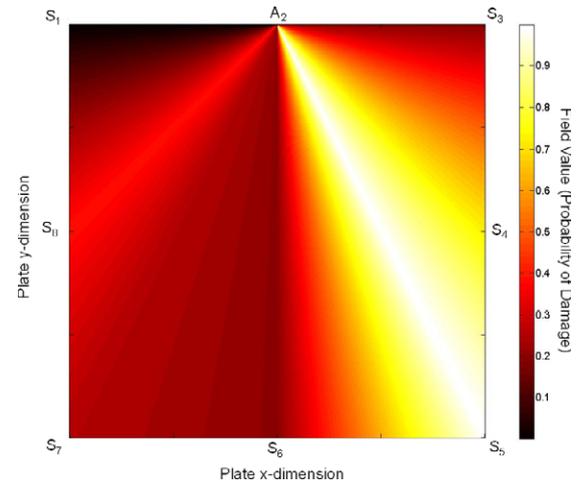

Figure 14. Source image established by physical sensing paths $A_2 - S_j$ ($j = 1, 3, \ldots, 7, 8$) and virtual sensing paths (diagram showing inspection area only covered by the sensor network).

Figure 13. Current and baseline signals acquired via pitch–catch sensing path $A_2 - S_5$ (normalized by the magnitude of baseline signal).

where $P_{\text{pulse–echo}}$ and $P_{\text{pitch–catch}}$ are the field values in their respective ultimate resulting images, shown in figures 15(b) and (c). It can be seen that the fusion using sole pulse–echo paths, figure 15(b), enables an approximate depiction of the damage shape by roughly highlighting the orientation of two crack edges, but a number of pseudo-damage locations (false alarms) are included in the image; the one using sole pitch–catch paths, figure 15(c), on the whole pinpoints the location of the damaged zone but fails to describe the damage shape under the interference of a great deal of noise. Unsatisfactory identification results as seen in figures 15(b) and (c) are attributable to the nature of arithmetic fusion in equation (9), through which all prior perceptions from individual sensing paths including noise are equally amalgamated and reflected in the ultimate resulting images. With an increase in involved sensing paths (more source images), damage-associated information is de-emphasised and meanwhile noise/uncertainties irrelevant to damage stand out in the ultimate image. In contrast, the hybrid fusion, figure 15(a), is able to accurately highlight the location, orientation, shape and size of two individual edges, efficiently screening false alarms. Such a capacity of hybrid fusion is due to the facts that (i) the arithmetic fusion in the scheme guarantees a full inclusion of prior perceptions from all individual source images and (ii) the conjunctive operation remains commonality in all source images (damage-associated signal features) and screens out random components (noise in individual source images).

4.2. Polygonal damage (multi-edge damage)

As an extension of the above application, the approach was used to identify polygonal damage formed by five edges (edges I, II, III, IV and V) in an aluminum plate with the same dimensions and sensor network configuration, as seen in figure 16. Five damage edges have different lengths (25, 25, 21, 22 and 22 mm, respectively) and angles relative to the x axis (65°, 133°, 41°, 92.5° and 168°, respectively).

actuator and α_{virtual} varied in the range of $[0, \pi]$ relative to the x axis, with known field values along seven physical sensing paths $A_2 - S_j$ ($j = 1, 3, \ldots, 7, 8$). Applied with the hybrid image fusion scheme defined by equation (8), all source images established by pulse–echo and pitch–catch paths in the sensor network were fused and the ultimate resulting image is shown in figure 15(a).

To further examine the effectiveness of the hybrid fusion, source images provided by sole pulse–echo paths and by sole pitch–catch paths, respectively, were fused in accordance with a pure arithmetic fusion scheme as

$$P_{\text{pulse–echo}} = \frac{1}{N} \sum_{i=1}^{N} I'_i|_{\text{I}} \qquad \text{(for eight pulse–echo paths)},$$
$$(9a)$$

$$P_{\text{pitch–catch}} = \frac{1}{N} \sum_{i=1}^{N} I_i|_{\text{II}} \qquad \text{(for eight actuators)}, \qquad (9b)$$
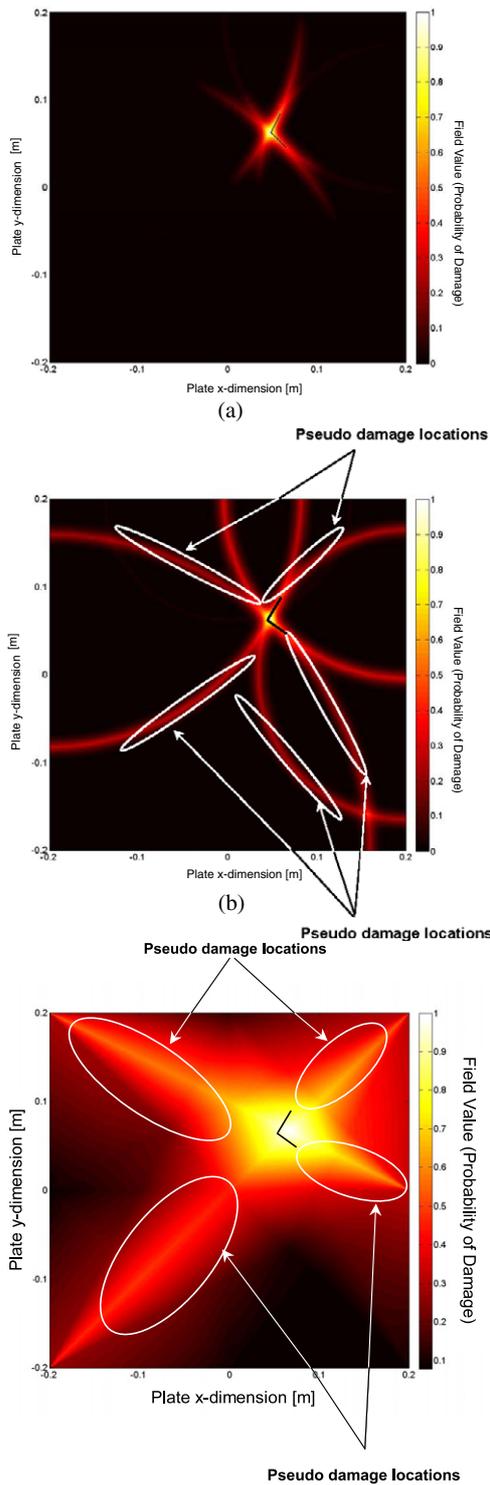
(a)

(b)

Figure 15. Ultimate resulting images for L-shape crack using (a) hybrid fusion scheme, (b) sole pulse–echo configuration and (c) sole pitch–catch configuration (diagram showing inspection area only covered by the sensor network; short black line: real edge of L-shape crack; white ellipse: area containing most pseudo-damage locations).

A fused image using the sole pulse–echo configuration is displayed in figure 17, rendering a limited description of damage shape, in which only edges I, II and III can be
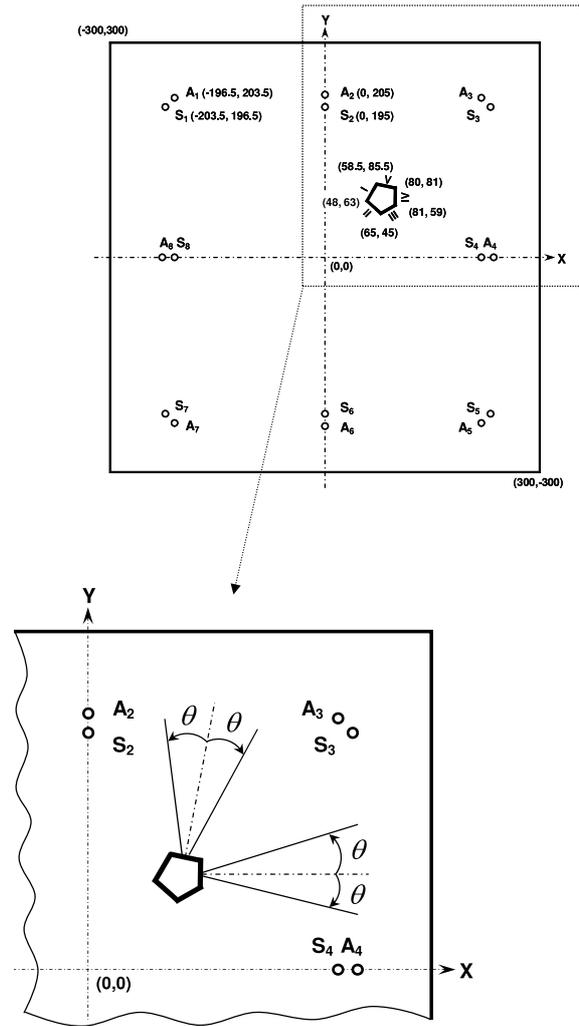

Figure 16. Specimen configuration for identifying polygonal damage (unit: mm) (PZT wafers in the sensor network being symmetric relative to *x* and *y* axes; insert: sensitive areas of edges IV and V).

highlighted. Abundant pseudo-damage locations are noticed in the image. The pseudo-damage can be seen to even hold higher probabilities of presence than actual damage (reflected by the higher field values (the first genre) at pixels in those circled areas). Such a deficiency of fusion indicates that the effectiveness of the approach may be jeopardized if only the information acquired via pulse–echo configuration was relied on.

In parallel, fused images using the sole pitch–catch configuration without and with the assistance of 'virtual sensing' are displayed in figures 18(a) and (b), respectively. In figure 18(a), pixels along physical paths, $A_1 - S_4$, $A_2 - S_5$ and $A_3 - S_7$ can be seen to hold higher field values (the second genre), implying a higher possibility of damage presence along these three sensing paths. As commented previously, the way to define the second genre of field value in terms of equation (5) makes a sensing path very sensitive to the damage near it, while highly inert to damage which is distant from it. When fused with other pitch–catch paths, these three paths became dominant. With such limited information, the identified results
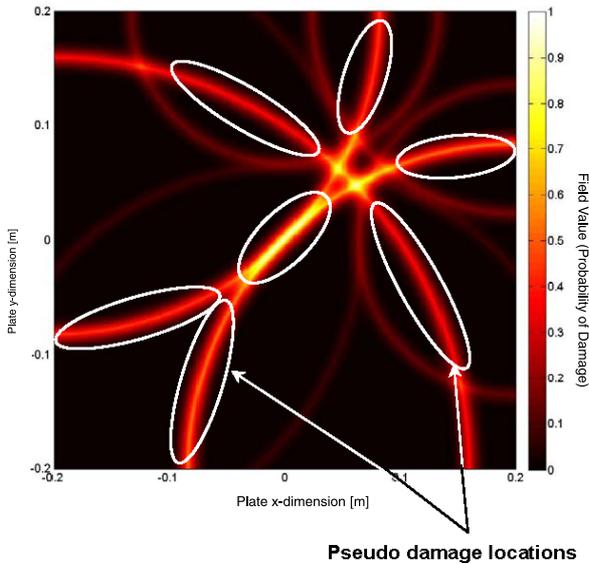
Figure 17. Ultimate resulting image for polygonal damage using sole pulse–echo paths (diagram showing inspection area only covered by the sensor network; white ellipse: area containing most pseudo-damage locations).

in figure 18(a) fail to quantitatively describe the multi-edge damage. On the other hand, using the concept of 'virtual sensing', the sensor network was virtually densified. As a direct result, prior perceptions from individual source images were well decentralized and noise was largely removed. As seen in figure 18(b), apart from an indication of damage location, an approximate depiction of the size of the polygonal damage was also achieved. But it is noteworthy that, although use of virtual sensing can compensate for insufficient source images, the fusion using sole pitch–catch configuration does not have a capacity of pinpointing individual damage edges, and the predicted damage shape shown in figure 18(b) largely deviates from reality.

Applied with the hybrid fusion scheme, figure 19(a) shows the ultimate resulting image, to observe that common perceptions of source images were intensified, whilst noise in each source image was suppressed considerably. Full geometric details of edges I, II and III are ascertained, and rough locations of edges IV and V can be recognized but with dim depiction on the edge orientation and length. This is attributable to the fact that each orientation-specific edge possesses a sensitive region in which the angle of wave incidence (θ in figure 5) is sufficiently small, so as to ensure the damage-scattered wave energy is captured efficiently by at least one pulse–echo sensing path. According to figure 5, the sensitive regions of edges IV and V are indicated in the insert of figure 16. With the current sensor network configuration, there is no pulse–echo sensing path passing through the sensitive regions of edges IV and V, making it difficult to identify these two edges provided the sole pulse–echo-configuration-based first genre of field value is used. Furthermore, if 50% of the maximum field value in the ultimate resulting image is set as a threshold to draw a definitive conclusion that damage occurs, the shape of the polygonal damage can be clearly depicted, as
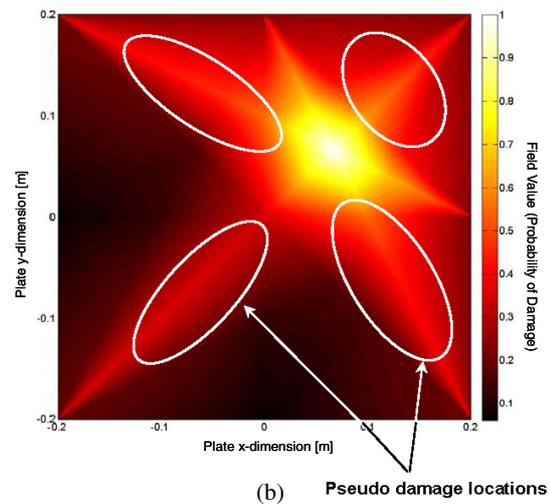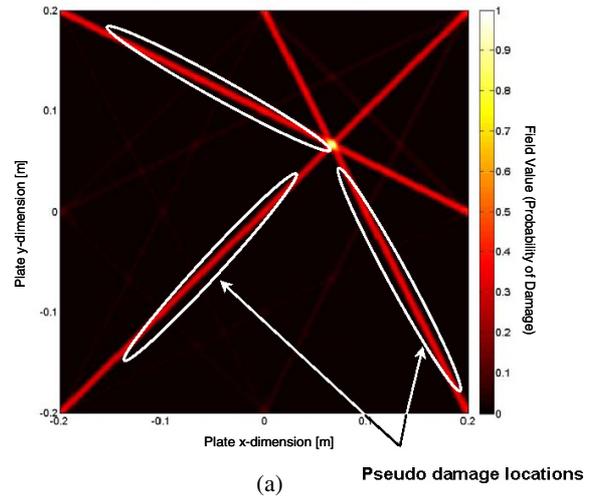

(a)

(b)

Figure 18. Ultimate resulting image for polygonal damage using sole pitch–catch paths (a) without and (b) with the assistance of virtual sensing (diagram showing inspection area only covered by the sensor network; white ellipse: area containing most pseudo-damage locations).

shown in figure 19(b), upon forcing all field values which are less than this threshold to be zero. In this case, the description on edges I, II and III becomes more legible, but edges IV and V are further hidden because the field values of those pixels located on these two edges in the ultimate image are less than the threshold. But at any rate, locations of all edges of the polygonal damage were ascertained using the hybrid fusion scheme.

4.3. Multi-damage

To identify multi-damage within the same inspection area is usually a tanglesome task, due to the challenge and difficulty in isolating different waves scattered from multi-damage. To examine the feasibility of the developed PDI approach in identifying multi-damage, the aluminum panel bearing the polygonal damage used in the above case was introduced with a through-thickness crack, referring to figure 20 (20 mm in length and 0.64 mm in width). In the developed PDI, natures of
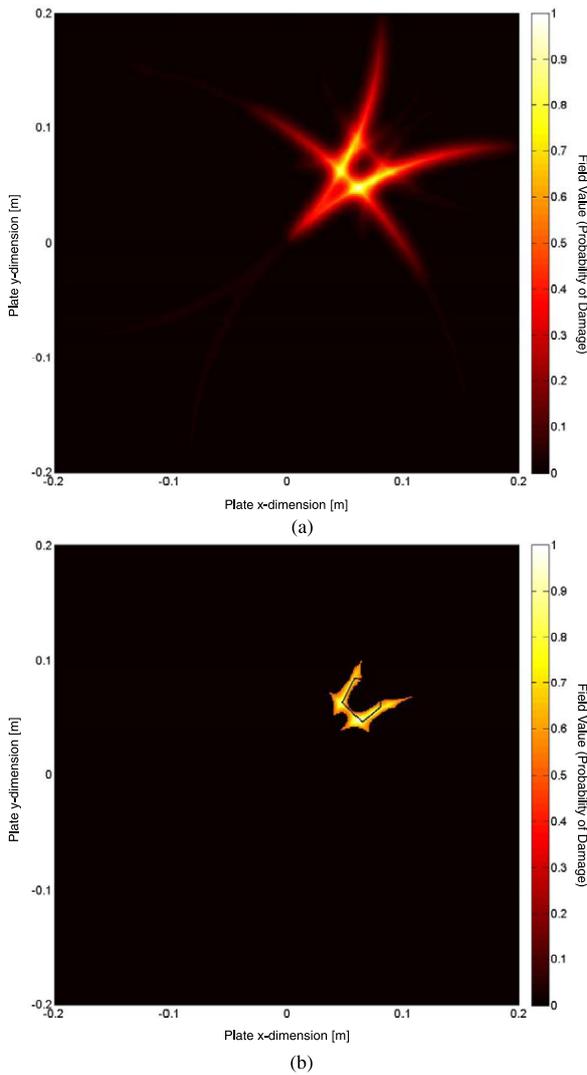
(a)

(b)

Figure 19. (a) Ultimate resulting image for polygonal damage using hybrid fusion scheme and (b) image in (a) upon applying a threshold of 0.5 (diagram showing inspection area only covered by the sensor network; short black line: real edge of polygonal damage).

Figure 20. Specimen configuration for identifying multi-damage (unit: mm) (PZT wafers in the sensor network being symmetric relative to *x* and *y* axes).

the first and second genres of field value endow a sensing path to perceive the damage most sensitively near it only. Such a trait can be beneficial to detecting multi-damage. For example, pairs $A_1 - S_1$ and $A_1 - S_4$ in this application offer crucial information for the polygonal damage, while pairs $A_8 - S_8$ and $A_6 - S_8$ provide more information regarding the crack. Furthermore, with the concept of 'virtual sensing', this active sensor network was expanded virtually, able to provide larger coverage and avoid insufficient acquisition of signal features. With the hybrid image fusion scheme, the ultimate resulting image is exhibited in figure 21(a). Similar as in section 4.2, with a pre-set threshold (50% of the maximum field value in the ultimate resulting image), all damage cases are depicted accurately and quantitatively, figure 21(b), including damage locations, shapes and sizes, matching well the reality.

In all the above three applications, it can be seen that the image fusion plays an essential role in PDI in screening unwanted signal features and standing out damage-associated
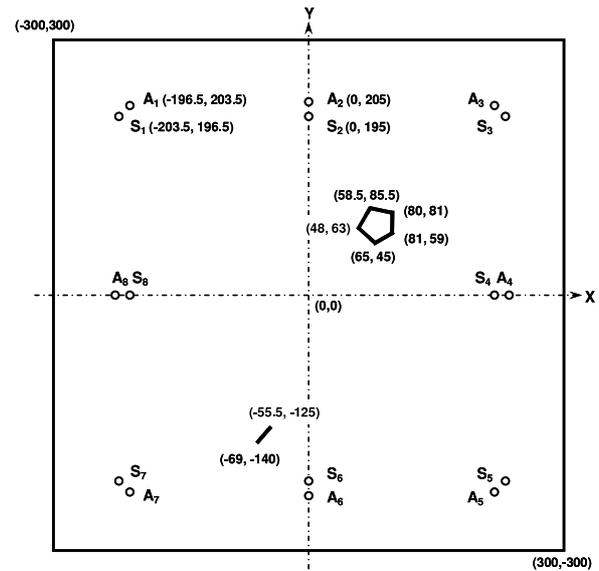
features. It facilitates a phenomenal improvement in the tolerance and robustness of PDI to measurement noise and uncertainties, as well as erroneous perceptions from individual sensing paths. It is also noteworthy that, in principle, an elastic-wave-based identification approach can detect damage that is greater than half the size of the wavelength. Generally speaking, the higher an excitation frequency, the smaller is the detectable damage, which however is at the expense of more dispersion of the generated Lamb waves. Therefore it is important to select an optimal frequency in practical implementation, so as to achieve a suitable compromise between damage detectability and signal recognizability. That is the reason why a frequency of 450 kHz was selected in this study, at which the wavelength of the selected wave mode was around 6.7 mm, enabling damage of 3.4 mm or more in dimension to be detected.

5. Conclusion

Hybrid signal features including ToF, intensity of signal energy and signal correlation were extracted from captured Lamb wave signals with the assistance of an active sensor network and a novel concept—'virtual sensing'. Various signal features were integrated to develop a retrofitted PDI approach. A hybrid image fusion scheme was developed, able to enhance the tolerance of the approach to measurement noise and possible erroneous perceptions from individual sensing paths. Satisfactory identification results for three selected damage cases, including L-shape through-thickness crack (strong orientation-specific damage), polygonal damage (multi-edge damage) and multi-damage in structural plates, have demonstrated the effectiveness of the developed PDI approach in quantitatively visualizing structural damage in an easily interpretable binary image by highlighting individual damage edges, regardless of its shape and number. However,
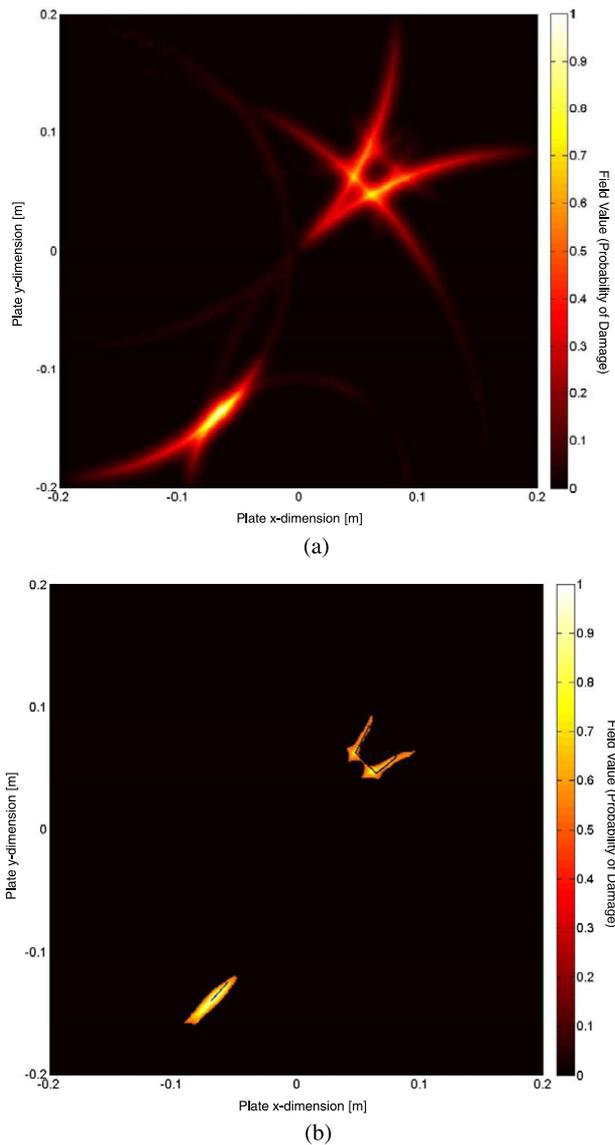
Figure 21. (a) Ultimate resulting image for multi-damage using hybrid fusion scheme and (b) image in (a) upon applying a threshold of 0.5 (diagram showing inspection area only covered by the sensor network; short black line: real edge of damage).

inefficiency of the approach has also been observed for some extreme cases in which there is no effective sensing path passing through the sensitive region of the damage. To include more signal features by taking full advantage of the sensor network is anticipated to circumvent this problem, constituting the ongoing efforts of the authors. Conclusions have also articulated that a judicious selection of image fusion scheme is crucial for a PDI technique to deliver precise and accurate identification.

Acknowledgments

References

[1] Sohn H and Lee S J 2010 Lamb wave tuning curve calibration for surface-bonded piezoelectric transducers *Smart Mater. Struct.* **19** 015007
[2] Lin B and Giurgiutiu V 2006 Modeling and testing of PZT and PVDF piezoelectric wafer active sensors *Smart Mater. Struct.* **15** 1085–93
[3] Fromme P, Wilcox P D, Lowe M J S and Cawley P 2006 On the development and testing of a guided ultrasonic wave array for structural integrity monitoring *IEEE Trans. Ultrason. Ferroelectr. Freq. Control* **53** 777–85
[4] Raghavan A and Cesnik C E S 2007 Review of guided-wave structural health monitoring *Shock Vib. Digest* **39** 91–114
[5] Kundu T, Das S and Jata K V 2009 Health monitoring of a thermal protection system using Lamb waves *Struct. Health Monit.* **8** 29–45
[6] Wang L and Yuan F G 2005 Damage identification in a composite plate using prestack reverse-time migration technique *Struct. Health Monit.* **4** 195–211
[7] Inman D J, Farrar C R, Lopes V Jr and Steffen V Jr 2005 *Damage Prognosis: for Aerospace, Civil and Mechanical Systems* (Hoboken, NJ: Wiley)
[8] Birt E A 2002 Application of ultrasonic Lamb waves for damage detection in carbon fibre composite aerospace structures *Insight* **44** 423–7
[9] Ryles M, Ngau F H, McDonald I and Staszewski W J 2008 Comparative study of nonlinear acoustic and Lamb wave techniques for fatigue crack detection in metallic structures *Fatigue Fract. Eng. Mater. Struct.* **31** 674–83
[10] McKeon J C P and Hinders M K 1999 Parallel projection and crosshole Lamb wave contact scanning tomography *J. Acoust. Soc. Am.* **106** 2568–77
[11] Leonard K R, Malyarenko E V and Hinders M K 2002 Ultrasonic Lamb wave tomography *Inverse Problems* **18** 1795–808
[12] Rosalie C, Chan A, Chiu W K, Galea S C, Rose F and Rajic N 2005 Structural health monitoring of composite structures using stress wave methods *Compos. Struct.* **67** 157–66
[13] Su Z, Wang X, Cheng L, Yu L and Chen Z 2009 On selection of data fusion schemes for structural damage evaluation *Struct. Health Monit.* **8** 223–41
[14] Su Z, Cheng L, Wang X, Yu L and Zhou C 2009 Predicting delamination of composite laminates using an imaging approach *Smart Mater. Struct.* **18** 074002
[15] Ihn J-B and Chang F-K 2008 Pitch-catch active sensing methods in structural health monitoring for aircraft structures *Struct. Health Monit.* **7** 5–19
[16] Michaels J E 2008 Detection, localization and characterization of damage in plates with an *in situ* array of spatially distributed ultrasonic sensors *Smart Mater. Struct.* **17** 035035
[17] Konstantinidis G, Drinkwater B W and Wilcox P D 2006 The temperature stability of guided wave structural health monitoring systems *Smart Mater. Struct.* **15** 967–76
[18] Wang C H, Rose J T and Chang F-K 2004 A synthetic time-reversal imaging method for structural health monitoring *Smart Mater. Struct.* **13** 415–23
[19] Wang Q and Yuan S F 2009 Baseline-free imaging method based on new PZT sensor arrangements *J. Intell. Mater. Syst. Struct.* **20** 1663–73

[20] Michaels J E and Michaels T E 2007 Guided wave signal processing and image fusion for *in situ* damage localization in plates *Wave Motion* **44** 482–92

[21] Zhao X, Gao H, Zhang G, Ayhan B, Yan F, Kwan C and Rose J L 2007 Active health monitoring of an aircraft wing with embedded piezoelectric sensor/actuator network: I. Defect detection, localization and growth monitoring *Smart Mater. Struct.* **16** 1208–17

[22] Ostachowicz W, Kudela P, Malinowski P and Wandowski T 2008 Damage localisation in plate-like structures based on PZT sensors *Mech. Syst. Signal Process.* **23** 1805–29

[23] Wang D, Ye L, Su Z, Lu Y, Li F and Meng G 2010 Probabilistic damage identification based on correlation analysis using guided wave signals in aluminium plates *Struct. Health Monit.* **9** 133–44

[24] Giurgiutiu V and Bao J 2004 Embedded-ultrasonics structural radar for *in situ* structural health monitoring of thin-wall structures *Struct. Health Monit.* **3** 121–40

[25] Zhou C, Su Z and Cheng L 2011 Quantitative evaluation of orientation-specific damage using elastic waves and probability-based diagnostic imaging *Mech. Syst. Signal Process.* **25** 2135–56

[26] Yan F, Royer R L Jr and Rose J L 2010 Ultrasonic guided wave imaging techniques in structural health monitoring *J. Intell. Mater. Syst. Struct.* **21** 377–84

[27] Staszewski W J and Worden K 2004 *Health Monitoring of Aerospace Structures: Smart Sensor Technologies and Signal Processing* ed W J Staszewski, C Boller and G R Tomlinson (Chichester: Wiley) chapter 5 (Signal Processing for Damage Detection) pp 163–206